Draft version August 9, 2018
Preprint typeset using LaTeX style emulateapj v. 5/2/11

STRUCTURAL EVOLUTION OF EARLY-TYPE GALAXIES TO Z=2.5 IN CANDELS

Yu-Yen Chang[1], Arjen van der Wel[1], Hans-Walter Rix[1], Bradford Holden[2], Eric F. Bell[3], Elizabeth J. McGrath[4], Stijn Wuyts[5], Boris Häussler[6], Marco Barden[7], S. M. Faber[2], Mark Mozena[2], Henry C. Ferguson[8], Yicheng Guo[2], Audrey Galametz[9], Norman A. Grogin[8], Dale D. Kocevski[2], Anton M. Koekemoer[8], Avishai Dekel[10], Kuang-Han Huang [8,11], Nimish P. Hathi [12], and Jennifer Donley [13]

Draft version August 9, 2018

ABSTRACT

Projected axis ratio measurements of 880 early-type galaxies at redshifts $1 < z < 2.5$ selected from CANDELS are used to reconstruct and model their intrinsic shapes. The sample is selected on the basis of multiple rest-frame colors to reflect low star-formation activity. We demonstrate that these galaxies as an ensemble are dust-poor and transparent and therefore likely have smooth light profiles, similar to visually classified early-type galaxies. Similar to their present-day counterparts, the $z > 1$ early-type galaxies show a variety of intrinsic shapes; even at a fixed mass, the projected axis ratio distributions cannot be explained by the random projection of a set of galaxies with very similar intrinsic shapes. However, a two-population model for the intrinsic shapes, consisting of a triaxial, fairly round population, combined with a flat ($c/a \sim 0.3$) oblate population, adequately describes the projected axis ratio distributions of both present-day and $z > 1$ early-type galaxies. We find that the proportion of oblate versus triaxial galaxies depends both on the galaxies' stellar mass, and - at a given mass - on redshift. For present-day and $z < 1$ early-type galaxies the oblate fraction strongly depends on galaxy mass. At $z > 1$ this trend is much weaker over the mass range explored here ($10^{10} < M_*/M_\odot < 10^{11}$), because the oblate fraction among massive ($M_* \sim 10^{11} M_\odot$) was much higher in the past: 0.59 ± 0.10 at $z > 1$, compared to 0.20 ± 0.02 at $z \sim 0.1$. When combined with previous findings that the number density and sizes of early-type galaxies substantially increase over the same redshift range, this can be explained by the gradual emergence of merger-produced elliptical galaxies, at the expense of the destruction of pre-existing disks that were common among their high-redshift progenitors. In contrast, the oblate fraction among low-mass early-type galaxies ($\log(M_*/M_\odot) < 10.5$) increased toward the present, from 0.38 ± 0.11 at $z > 1$ to 0.72 ± 0.06 at $z = 0$. We speculate that this lower incidence of disks at early cosmic times can be attributed to two factors: low-mass, star-forming progenitors at $z > 1$ were not settled into stable disks to the same degree as at later cosmic times, and the stripping of gas from star-forming disk galaxies in dense environments is an increasingly important process at lower redshifts.

Subject headings: galaxies: evolution — galaxies: formation — galaxies: structure — galaxies: elliptical and lenticular, cD — cosmology: observations

1. INTRODUCTION

Early-type galaxies show a large variety in spatial and kinematic structure (e.g., Kormendy & Bender 1996; Emsellem et al. 2011, and references therein). Among early types with typical luminosities (L^*) or stellar masses, most have disk-like properties in that they are axisymmetric, rotating and intrinsically flat, even though their light profiles are significantly more concentrated than those of late-type, star-forming L_* galaxies. More massive early-type galaxies are rounder, triaxial, and slowly rotating. Given these fundamental differences, one may surmise that disk-like and spheroid-dominated galaxies have different evolutionary paths and formation mechanisms. Here we empirically address this issue by analyzing the shape distribution of early-type galaxies as a function of redshift. Our reconstruction of the internal structure of early-type galaxies at different cosmic epochs will provide insight into the assembly history of massive, triaxial galaxies as well as the evolutionary path of less massive, disk-like early-type galaxies.

The internal structure of galaxies has been studied by means of analyzing projected shape distributions for several decades. Early on, axisymmetric structure was assumed to describe the three-dimensional

[1] Max-Planck Institut für Astronomie, Königstuhl 17, D-69117, Heidelberg, Germany; e-mail: chang@mpia.de
[2] UCO/Lick Observatory, Department of Astronomy and Astrophysics, University of California, Santa Cruz, CA 95064, USA
[3] Department of Astronomy, University of Michigan, 500 Church Street, Ann Arbor, MI 48109, USA
[4] Department of Physics and Astronomy, Colby College, Waterville, ME 04901, USA
[5] Max-Planck-Institut für Extraterrestrische Physik, Postfach 1312, Giessenbachstr., D-85741 Garching, Germany
[6] Schools of Physics & Astronomy, University of Nottingham, University Park, Nottingham NG7 2RD, UK
[7] Institute of Astro- and Particle Physics, University of Innsbruck, Technikerstraße 25, A-6020 Innsbruck, Austria
[8] Space Telescope Science Institute, 3700 San Martin Drive, Baltimore, MD 21218, USA
[9] INAF - Osservatorio di Roma, Via Frascati 33, I-00040, Monteporzio, Italy
[10] Racah Institute of Physics, The Hebrew University, Jerusalem 91904 Israel
[11] Department of Physics and Astronomy, Johns Hopkins University, Baltimore, MD 21218, USA
[12] Observatories of the Carnegie Institution for Science, Pasadena, CA, USA
[13] Los Alamos National Laboratory, Los Alamos, NM, USA

light profile of galaxies, that is, the projection of simple oblate and prolate models was used (Hubble 1926; Sandage et al. 1970; Binney 1978; Fall & Frenk 1983). Then the triaxial model family (Stark 1977; Binney 1985; Franx et al. 1991) was considered to account for observational evidence that local early-type galaxies are not axisymmetric (Ryden 1992; Lambas et al. 1992; Tremblay & Merritt 1995; Kimm & Yi 2007; Padilla & Strauss 2008; Mèndez-Abreu et al. 2010). Tremblay & Merritt (1996) showed that the projected axis ratio distribution of early-type galaxies is accurately described by a model that consists of an oblate and a triaxial set of objects. Brighter galaxies tend to be more triaxial (non-axisymmetric) than fainter galaxies, which are more axisymmetric and intrinsically flatter (Vincent & Ryden 2005). This two-component model does not provide a mathematically unique solution, but is physically plausible, in line with the kinematic distinction of 'fast rotators' and 'slow rotators' (e.g., Emsellem et al. 2011).

van der Wel et al. (2009, hereafter vdW09) used stellar masses instead of luminosity, and described the projected axis ratio distribution of early-type galaxies. In addition to enabling a more immediate comparison with galaxy formation models, the use of stellar masses instead of luminosities simplifies the interpretation of evolution with redshift (Holden et al. 2012, hereafter H12) (also see Holden et al. 2009) vdW09 and H12 found that at all redshifts $z \lesssim 1$ there is a quite sudden transition in the projected axis ratio distribution at a stellar mass of $\sim 10^{11} M_{\odot}$. At lower masses the projected axis ratio distribution is broad, indicative of a large fraction of disk-like early-type galaxies, which have a ceiling mass of $\sim 2 \times 10^{11} M_{\odot}$, above which essentially all early-type galaxies are intrinsically round. H12 provide a quantitative analysis by describing the projected axis ratio distribution of early-type galaxies, and its evolution with redshift by the aforementioned two-component model. Overall, they found little evolution between $z = 0.8$ and the present. van der Wel et al. (2011) and Chang et al. (2013, hereafter C13) extended these studies to higher redshift. They found that massive early-type galaxies at $z \gtrsim 1.5$ are flatter than at the present. Their implied disk-like structures show that these galaxies formed while gas had time to settle into disks.

The vdW09, H12, and C13 samples were selected by (a lack of) star formation activity (also see Wuyts et al. 2007; Williams et al. 2009). Such a selection can effectively be used as a proxy for a (visual) morphological classification, as a smooth light profile is the main criterion for the visual classification of an early-type galaxy, which usually corresponds to low star-formation activity (also see Patel et al. 2012). A practical advantage of a star formation selection is that it allows for the consistent selection of high-redshift samples, for which visual classification is difficult or impossible. Furthermore, since we are investigating the evolution of structural properties, the use of structural parameters such as concentration or Sérsic index to select early-type galaxies are prone to introducing biases.

So far, these results have been rather qualitative. In this paper, we provide a more quantitative description of the internal structure of $z = 1 - 2.5$ early-type galaxies down to $M \sim 10^{10}$. The Cosmic Assembly Near-infrared Deep Extragalactic Legacy Survey (CANDELS, Grogin et al. 2011; Koekemoer et al. 2011), a 902 orbit Hubble Space Telescope (HST) multi-cycle treasury program, provides high-resolution near-infrared imaging aimed at investigating the structural and morphological properties of galaxies to $z \sim 3$ in the rest-frame optical. van der Wel et al. (2012, hereafter vdW12) used `GALFIT` (Peng et al. 2010) to measure the global structural parameters of $\sim$ 100,000 galaxies in CANDELS. We draw from this work to construct a sample of 569 $z > 1$ early-type galaxies with accurately measured axis ratios.

The structure of this paper is as follows. In Section 2 we describe the data and select our sample of early-type galaxies. In Section 3 we analyze the structural parameters of early-type galaxies and their evolution since $z \sim 2.5$ and as a function of stellar mass. In Section 4 we describe our models to reconstruct the intrinsic shape distribution. In Section 5 we investigate the internal structure of early-type galaxies and its evolution. In Section 6 and 7 we discuss and summarize our results.

We use AB magnitudes and adopt the cosmological parameters (Ω_M,Ω_Λ,h)=(0.27,0.73,0.70) in this paper.

2. DATA

2.1. *Multi-wavelength Data and SED Fitting*

In this paper, we use imaging and multi-wavelength catalogs from CANDELS in the Great Observatories Origins Deep Survey-South field (GOODS-S, Giavalisco et al. 2004, 'wide' over 4'×10' and 'deep' over 7×10') and Ultra Deep Survey field (UDS; Lawrence et al. 2007, wide over 9'×24'). The deep near-infrared HST survey allows us to select early-type galaxies up to $z = 2.5$. The details of the multi-wavelength catalogs are described in Guo et al., (2013, GOODS-S), Galametz et al. (2013, UDS), and Ashby et al. (2013, IRAC SEDS catalog).

The method and algorithms for acquiring photometric redshifts, rest-frame colors and stellar masses are described by Wuyts et al. (2011). Briefly, photometric redshifts are estimated by EAzY (Brammer et al. 2008) and available spectroscopic redshifts are included. The stellar masses, star-formation rates, and rest-frame colors are estimated by FAST (Kriek et al. 2009). The Bruzual & Charlot (2003) model, and a Chabrier (2003) stellar initial mass function is adopted. A range of ages, star formation histories and extinction parameters is explored.

2.2. *Galaxy Structural Parameters*

The structural parameters (radii, Sérsic indices and projected axis ratios) are taken from vdW12 who fit single Sérsic profiles to individual galaxies with `GALFIT`. Many of the galaxies in our sample are very small ($\sim$ 1kpc), close to the resolution limit. If the point spread function (PSF) is precisely known, this is not a problem as shown by vdW12, at least under the assumption that the characterization of the light profile by a single Sérsic component is reasonable. In order to test the sensitivity of our results to errors in the PSF model, we refit our sample with the 'wrong' PSF: if we convolve the Sérsic profile with the F125W PSF model in order to fit the F160W images, the resulting axis ratios are larger, but not to the extent that our results are affected. Since we

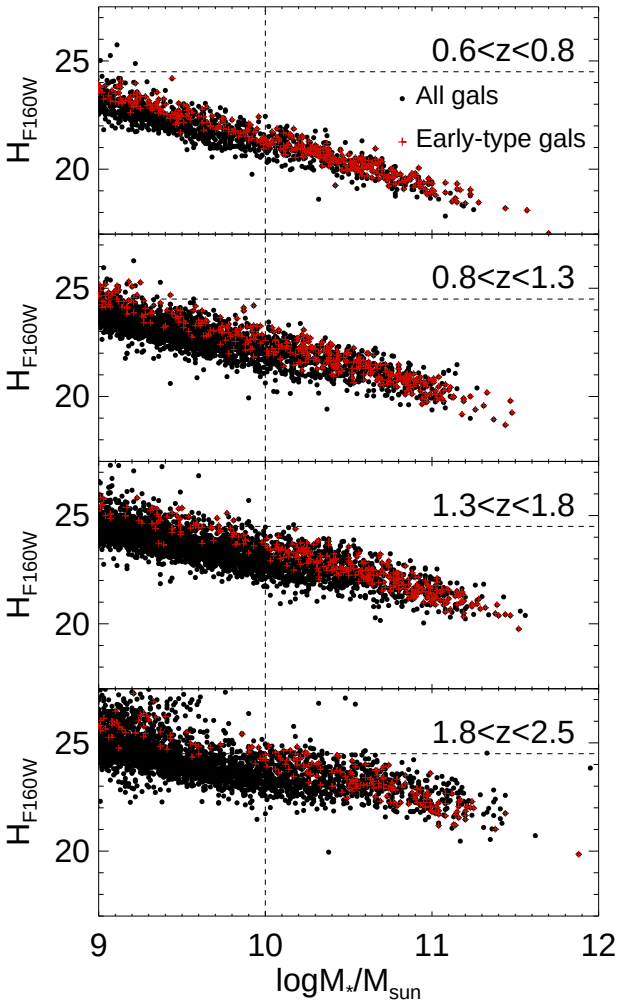

FIG. 1.— CANDELS H_{F160W} magnitude vs. stellar mass at different redshifts. The red crosses represent early-type galaxies, selected as described in Section 2.3 and illustrated in Figure 2. The black symbols represent all galaxies. We adopt $H_{F160W} = 24.5$ as our magnitude limit: vdW12 showed that size and shape measurements are better than 10% down to this limit. This leads us to adopt a stellar mass limit of $\log(M_*/M_\odot) > 10$, ensuring robust structural parameter estimates for all galaxies in our sample up to $z \sim 2.5$.

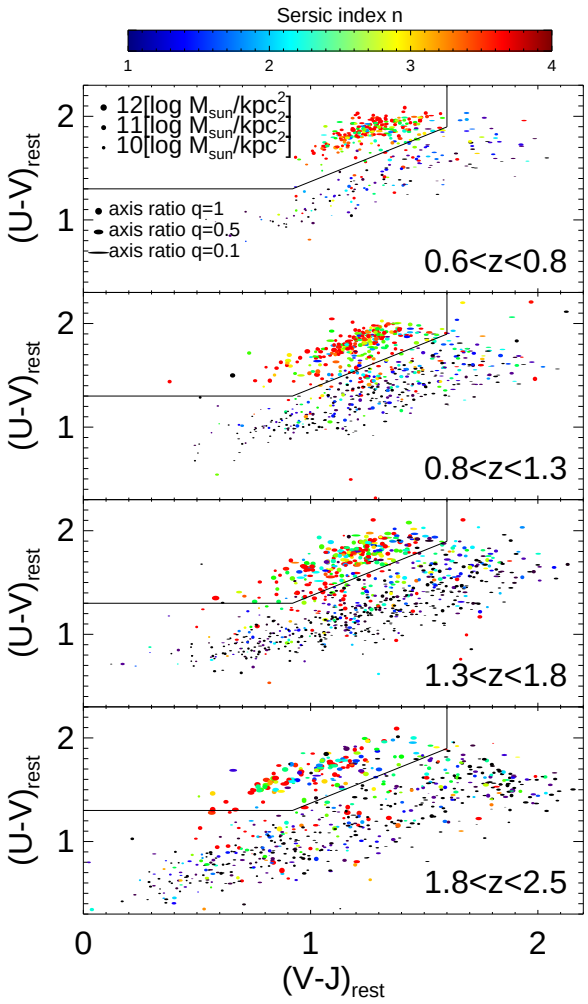

FIG. 2.— Rest-frame $U - V$ vs. rest-frame $V - J$ colors for galaxies in four redshift bins. As shown, e.g., by Williams et al. (2009), the black polygons effectively separate star-forming and quiescent galaxies, which we use in this paper to select our early-type sample. The symbols' color coding corresponds to the Sérsic index n, the symbol size (area) with stellar mass surface density ($M_*/2\pi q R_{\rm eff}^2$), and symbol shape with observed, projected axis ratio q. The color-color selection separation of early- and late-type galaxies corresponds well with their structural properties in the sense that early-type galaxies have high Sérsic indices and large surface mass densities.

know the F160W PSF with much better accuracy than the $\sim$ 15% difference between the F125W and F160W PSFs (FWHM$_{F125W}$ $\sim$ 0″.20; FWHM$_{F160W}$ $\sim$ 0″.17), we conclude that errors in our PSF model do not affect our results.

2.3. *Sample Selection*

Combining the multi-wavelength and structure parameter catalogs, we have an initial sample of 56,010 objects (21,889 in GOODS-S and 34,121 in UDS). Size and shape measurements are accurate and precise to 10% for galaxies with $H_{F160W} \sim 24.5$ (see vdW12). We adopt a stellar mass limit of $M = 10^{10} M_\odot$, which allows us to consistently compare galaxies at all redshift $z < 2.5$ (see Figure 1). We reject stars by including only objects with $J - H > 0.15$. We only include galaxies with good GALFIT fits (flag=0; 87% of the remaining sample) from the vdW12 catalog and ignore 13% with suspect fits (flag=1) or bad fits (flag=2). This mass-selected sample with reliable structure measurements consists of 2,827 objects.

To separate quiescent galaxies from star-forming galaxies, we use color-color selection criteria as shown in Figure 2, following: $(U - V) > 0.88 \times (V - J) + 0.49$, $(U - V) > 1.3$ and $(V - J) < 1.6$. [1] We define these as early-type galaxies and the remainder as late-types. This approach follows the technique outlined by, Williams et al. (e.g., 2009), but the color selection criteria are slightly different to account for differences in filter transmission curves and small offsets in the flux measurements. In Figure 2 it can be seen that this star-formation activity- based selection corresponds well with the Sérsic index, indicating that our selection by star formation ac-

[1] To compute the rest-frame U, V, and J band fluxes, we use the UX and V Bessell filters and the Palomar J filter.

tivity is effectively equivalent to a concentration-based definition of early type (also see Bell 2008; Wuyts et al. 2011; Bell et al. 2012; Wuyts et al. 2012) over the full redshift range probed here. As noted before, star-formation activity is strongly anti-correlated with Sérsic index and surface mass density, up to at least $z = 2.5$. Even though in this paper we emphasize the diskiness of early-type galaxies, it is also apparent in Figure 2 that late-type galaxies are still flatter, that is, more disk-like, than early-type galaxies at all redshifts.

The final sample of mass-selected early-type galaxies with reliable (flag=0) structure measurements consists of 880 galaxies in the redshift range $0.6 < z < 2.5$. The numbers of galaxies in different redshift bins are shown in Table 1. We create three stellar mass bins for CANDELS with a roughly equal number of galaxies.

TABLE 1
Sample Sizes

$\log(M_*/M_\odot)$	$10.1-11.5$	$10.8-11.5$	$10.5-10.8$	$10.1-10.5$
Redshift	Numbers			
SDSS	32842	13640	13991	5211
H12	1321	384	475	462
$1 < z < 2.5$	569	197	168	204
$0.6 < z < 0.8$	220	47	67	106
$0.8 < z < 1.3$	256	78	66	112
$1.3 < z < 1.8$	244	88	71	85
$1.8 < z < 2.5$	147	55	47	45

The SDSS sample from H12 is used as a low-redshift benchmark. Here, the early-type galaxies are selected by an equivalent color-color criterion. We verified that rejecting all SDSS color-color selected early-type galaxies with detected $H\alpha$ emission ($\sim 18\%$ of the sample) does not change our results. Even though the galaxies with detected emission lines are on average somewhat flatter than their counterparts without emission lines, the axis ratio distribution analyzed in the subsequent sections is not significantly altered.

Sufficiently deep emission-line data are not available for the galaxies in CANDELS. Instead, we search for detections in public MIPS 24μm imaging in the UDS[2] and cataloged MIPS 24μm flux measurements from Wuyts et al. (2008) in GOODS-S. Removing the 3σ detected objects ($\sim 16\%$) does not change the projected axis ratio distributions significantly. We conclude that the evolutionary trends with redshift are not sensitive to the inclusion of contaminating populations of star-forming galaxies and/or active galactic nuclei.

3. EVOLUTION OF THE PROJECTED AXIS RATIO DISTRIBUTION

In Figure 3 we show the axis-ratio distributions of early-type galaxies as a function of stellar mass for a number of redshift bins from $z = 0.6$ to $z = 2.5$. Half-light radii (R_{eff}) and Sérsic indices (n) are represented by varying the symbol size and color coding, respectively. Over the whole stellar mass range probed here the typical R_{eff} and n increase from $z \sim 2.5$ to later times, while non-starforming galaxies with exponential light profiles are rare at all redshifts. As previously reported by vdW09, H12, and C13, the most massive galaxies are the roundest, which can be seen here in particular at $z \sim 1$; at higher redshifts the probed volume is too small to include a sufficiently large number of very massive galaxies.

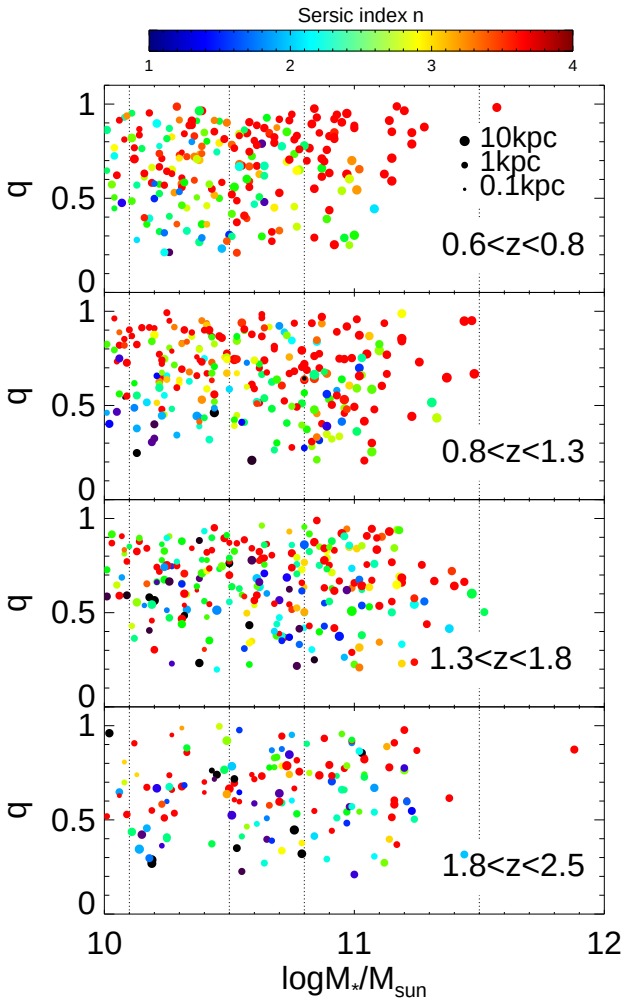

Fig. 3.— Projected axis ratio vs. stellar mass for early-type galaxies in CANDELS in four redshifts bins. The symbols' color coding corresponds to the Sérsic index n, the symbol size represents the radius in kiloparsecs. High-mass early-type galaxies are rounder and have higher Sérsic indices than low-mass early-type galaxies, but these trends apparently weaken at $z \sim 2$. At all redshifts, flatter galaxies have lower Sérsic indices, indicating that the population exists of a mix of different types of galaxies, and that variation in projected shape is not only the result of different viewing angles. The thin vertical lines indicate the mass bins that we use in this paper,
and are chosen to contain similar numbers of galaxies.

The main results presented in this paper can all be qualitatively seen in Figure 3. First, as was also shown by C13, there are many flat early-type galaxies with mass $\sim 10^{11} M_\odot$ at $z > 1$. Second, and contrarily, there are not many flat early-type galaxies with mass $\sim 10^{10} M_\odot$ at $z > 1$. The overall tendency is that the dependence of shape on galaxy mass is weak at $z > 1$ and strong at $z < 1$. To investigate these indications of structural evolution in a quantitative way, we will model the projected axis ratio distributions to infer the intrinsic shape distribution in Section 5.

[2]http://irsa.ipac.caltech.edu/data/SPITZER/SpUDS

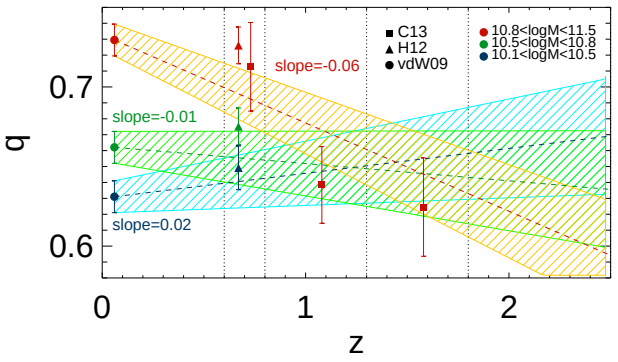

FIG. 4.— Evolution of the projected axis ratios for galaxies in three mass bins (color coding). The filled symbols are median values of previously published results. The dashed lines represent fits to the redshift-axis ratio distribution of the individual objects in the CANDELS sample, anchoring to the median axis ratio of present-day galaxies. The shaded area indicates the $1-\sigma$ uncertainty. See the text for details on the fitting method. The most significant evidence for evolution is seen for the massive galaxies: these are progressively flatter at higher redshift.

But first, we will establish the significance of these trends in a model-independent manner. In Figure 4, we perform least-squares fits to the axis ratios of the full $0.6 < z < 2.5$ sample separated into three mass bins, anchored by the low-redshift median values from the SDSS sample to which we assign a 0.01 systematic uncertainty (see H12). The uncertainties on the least-square fits are obtained by bootstrapping the sample and perturbing the photometric redshift (z_{phot}) and the projected axis ratio by their measurement uncertainties. Moreover, uncertainties in stellar masses (M_*) are included in two steps: first, the perturbation in photometric redshift is propagated ($M_* \propto (1+z)^4$) and, second, a random mass uncertainty of 0.2 dex (see, e.g., van der Wel et al. 2006) is included. Figure 4 shows that there is significant evolution in the projected axis ratios for massive galaxies, with the projected axis ratios decreasing toward high redshift, and we find marginal evidence for increasing projected axis ratios with redshift for the lowest-mass sample.

We now turn to the full distribution of axis ratios, which, compared to evolution in the average or median, enables more sensitive tests for structural evolution. In Figure 5, we compare the axis ratio distributions of our $1 < z < 2.5$ early-type galaxies with local early-type galaxies (see vdW09 and H12) by means of cumulative distributions and of histograms. Figure 5 shows that for $\log(M_*/M_\odot) > 10.8$, high-redshift galaxies are flatter (have smaller projected axis ratios) than local galaxies, while for $\log(M_*/M_\odot) < 10.5$, high-redshift galaxies are rounder. We use Kolmogorov-Smirnov (K-S) and Mann-Whitney U (M-W) tests to show that these trends are significant at the 5σ and 3σ level, respectively. These quantitative comparisons confirm the hints seen in Figure 3.

While the flattening of high-mass galaxies is consistent with previous results (van der Wel et al. 2011; Bruce et al. 2012; Whitaker et al. 2012; Buitrago et al. 2013, , and C13), the 3σ-level evidence that low-mass early types were rounder at earlier epochs is surprising. One could suspect that systematic shape measurement errors may prevent us from recovering the actual flatness of the small, faint galaxies in this sub-sample. However, the simulations performed by vdW12 indicate that shapes and sizes can be recovered with high accuracy down to the regime probed here. Note, however, that those simulations were performed with ideal Sérsic profiles, not with real galaxy light profiles. In addition, we can ask whether mismatches in the PSF model matter. In order to test this we rerun the profile fits on the F125W images of this sub-sample of low-mass early-type galaxies. For this test we replace the F125W PSF model, which we assume to be accurate, with the F160W PSF model. We know that the F160W PSF model is too broad to describe the light profiles of point sources in the F125W imaging (by $\sim 15\%$). Therefore, the projected axis ratio will now be underestimated (objects will appear flatter than they are). Even with this crudely wrong PSF model we find that the axis ratios of the low-mass $z > 1$ early types are not flatter than the axis ratios of their present-day counterparts. Given that the uncertainty in our PSF models is much smaller than the difference between the F125W and F160W PSF models, we can safely conclude that the observed evolution in the axis ratio distribution for low-mass early-type galaxies is not due to uncertainties in our PSF models.

Now we proceed in the next two sections to reconstruct the intrinsic structural properties of early-type galaxies as a function of stellar mass and redshift. We explore a variety of approaches that employ different model families and search for solutions by assuming random viewing angle distributions for our samples. In Section 4 we apply an analytical approximation to reconstruct the intrinsic axis ratio distribution of axisymmetric model families. In Section 5 we project model distributions that represent a combination of axisymmetric and triaxial families in order to reproduce the observed distributions of projected axis ratios and to find best-fitting solutions.

4. ANALYTICAL RECONSTRUCTION OF THE INTRINSIC SHAPE DISTRIBUTION

For an oblate ellipsoid at the origin of a Cartesian coordinate system, the intrinsic shape can be written as $x^2 + y^2 + z^2/\gamma^2 = 1$, where γ ($0 < \gamma \leq 1$) is the intrinsic axis ratio between the (one) short axis and the (two) long axes. For a prolate ellipsoid, the intrinsic shape can be written as $x^2/\gamma^2 + y^2/\gamma^2 + z^2 = 1$, where γ ($0 < \gamma \leq 1$) is the intrinsic axis ratio between the (two) short axes and the (one) long axis. The intrinsic axis-ratio distribution, $\psi(\gamma)$, can be inferred as prescribed by Fall & Frenk (1983):

$$\psi_O(\gamma) = \frac{2}{\pi}\sqrt{1-\gamma^2}\frac{d}{d\gamma}\int_0^q \frac{\phi_O(q)dq}{\sqrt{\gamma^2-q^2}} \quad (1a)$$

$$\psi_P(\gamma) = \frac{2}{\pi}\frac{\sqrt{1-\gamma^2}}{\gamma^2}\frac{d}{d\gamma}\int_0^q \frac{\phi_P(q)q^3dq}{\sqrt{\gamma^2-q^2}}, \quad (1b)$$

where ϕ is the projected axis-ratio distribution, and the subscripts O and P refer to the oblate and prolate case, respectively. If we describe the projected axis-ratio distribution by a power law ($\phi(q) = (m+1)q^m$ with

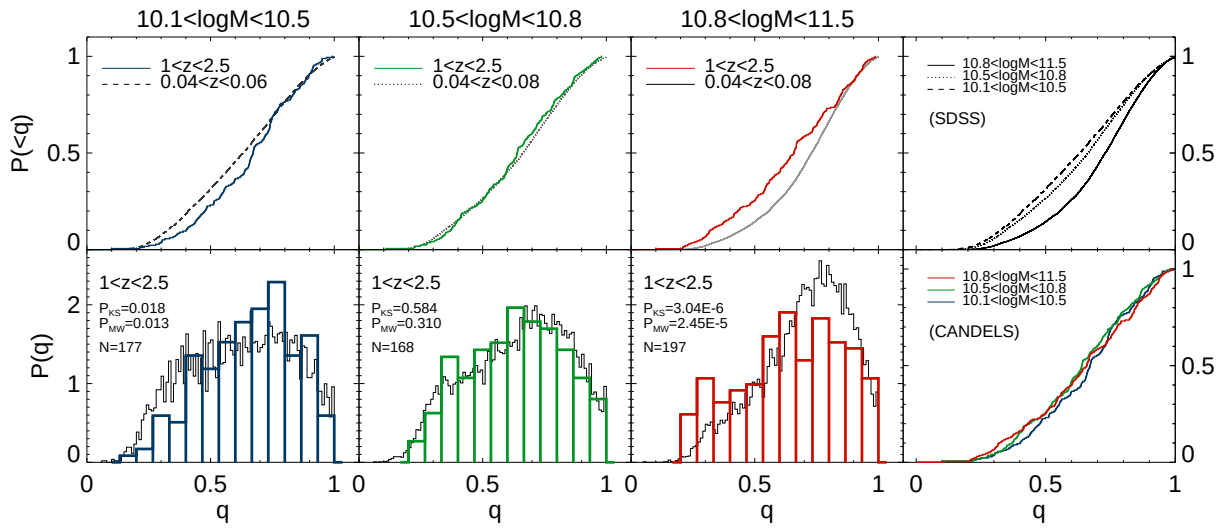

FIG. 5.— Redshift evolution of the projected axis ratio distributions in different mass bins. The top row of panels shows cumulative distributions; the bottom row shows binned histograms. The colored lines and histograms represent the $1 < z < 2.5$ CANDELS early-type galaxy sample; the gray/black lines represent the present-day early-type galaxy sample from SDSS. The right most panels combine the cumulative histograms for the present-day sample (top) and high-redshift sample (bottom), separated according to the mass bins. Probabilities that the distributions are consistent with each other from two statistical tests (Kolmogorov-Smirnov and Mann-Whithney) are given in the bottom panels. The samples high- and low-mass bins show evidence for evolution in opposite directions: whereas high-mass galaxies are flatter at high redshifts, low-mass galaxies are rounder.

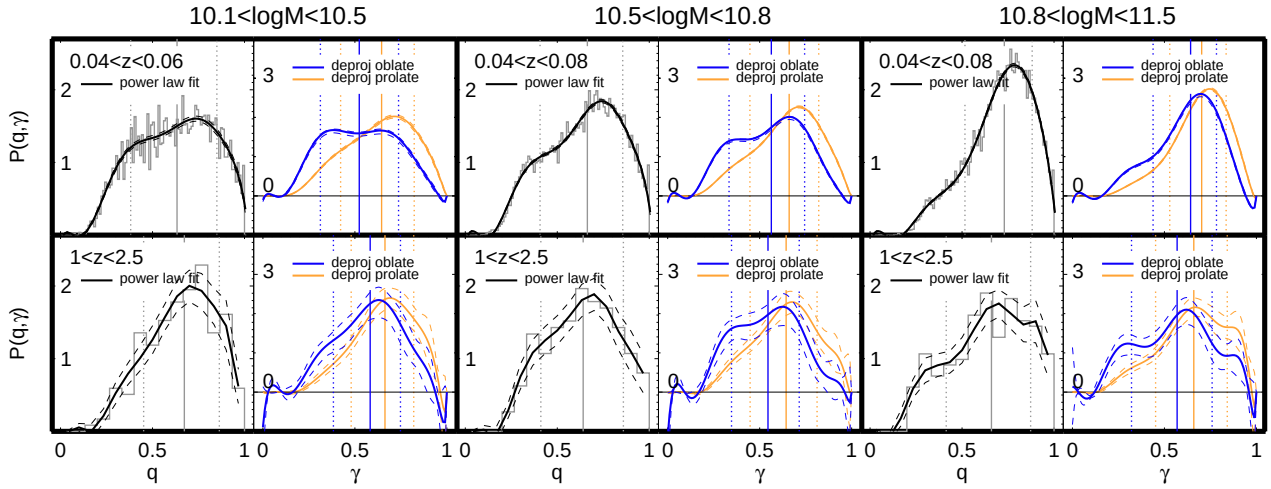

FIG. 6.— Projected axis ratio (q) distributions in gray/black and deprojected, intrinsic axis ratio (γ) distributions in blue/orange, inferred as described in Section 4. Observed, projected axis ratio distributions (black histograms) are represented by eighth-order polynomials (black lines) and then analytically deprojected according to Equation (1) to infer the intrinsic shape distribution of axisymmetric model populations (oblate in blue; prolate in orange). The dashed lines below and above the solid lines represent the 16 and 84 percentile confidence intervals obtained from bootstrapping ($n = 10,000$). The vertical lines show the 16, 50, and 84 percentiles of the deprojected intrinsic axis ratios. The top row of panels shows present-day early-type galaxies from SDSS; the bottom row shows $1 < z < 2.5$ early-type galaxies from CANDELS.

$m > -1$), we can rewrite Equation (1) analytically:

$$\psi_O(\gamma) = \frac{2\gamma^{m-1}\sqrt{1-\gamma^2}}{B(0.5m, 1.5)} \tag{2a}$$

$$\psi_P(\gamma) = \frac{2\gamma^{m}\sqrt{1-\gamma^2}}{B(0.5m+0.5, 1.5)}, \tag{2b}$$

where $B(x, y)$ is the beta function. The reconstructed intrinsic axis ratio distribution should be non-negative if an oblate or prolate model is a good description of the data.

4.1. *Application*

Figure 6 shows the results of the deprojection outlined above. We use an eighth-order power law, $\phi(q) = \Sigma_{m=0}^{8} C_m (m+1) q^m$, to describe the observed projected axis ratio distributions (black lines in Figure 6). The dashed lines show the 16 and 84 percentile confidence intervals obtained from bootstrapping (e.g., Tremblay & Merritt 1995, 1996; Ryden 1996a,b). The reconstructed intrinsic shape distributions for the oblate and prolate models (shown in thick blue and orange lines, respectively) are sometimes slightly negative, but the uncertainties are such that this can be attributed to the lim-

ited sample size. The distributions are very broad; that is, in narrow ranges of mass, galaxies display a large variety in intrinsic shape, and the population cannot consist of objects that are all similar in intrinsic thickness. This is true both for present-day galaxies and for $z > 1$ galaxies. Changes in the intrinsic shape distribution with redshift mirror changes in the projected shape distribution: high-mass galaxies were on average flatter at $z > 1$, and low-mass galaxies were rounder. Especially for the large, present-day samples, there is a clear hint that multiple components (galaxy populations) are needed to describe the intrinsic shape distribution, which we will explore below.

5. PROJECTION OF AXISYMMETRIC AND TRIAXIAL MODELS

Following Binney (1985) Equation (11) and (12), we project a triaxial ellipsoid (written as $m^2 = x^2/a^2 + y^2/b^2 + z^2/c^2$, at the origin of Cartesian coordinate system) and compute the projected axis ratio q as follows:

$$A = \frac{\cos^2\theta}{\gamma^2}\left(\sin^2\phi + \frac{\cos^2\phi}{\beta^2}\right) + \frac{\sin^2\theta}{\beta^2} \quad (3a)$$

$$B = \cos\theta \sin 2\phi \left(1 - \frac{1}{\beta^2}\right)\frac{1}{\gamma^2} \quad (3b)$$

$$C = \left(\frac{\sin^2\phi}{\beta^2} + \cos^2\phi\right)\frac{1}{\gamma^2} \quad (3c)$$

$$q(\theta,\phi;\beta,\gamma) = \sqrt{\frac{A + C - \sqrt{(A-C)^2 + B^2}}{A + C + \sqrt{(A-C)^2 + B^2}}}, \quad (3d)$$

where (θ,ϕ) are the polar and azimuthal viewing angles in a spherical coordinate system, and $\beta = b/a$ and $\gamma = c/a$. Note that $\beta = 1$ and $\beta = \gamma$ correspond to the special, axisymmetric cases (oblate and prolate, respectively). In order to account for variations in intrinsic shape, we assume a Gaussian distribution for the triaxiallity $T(= [1-\beta^2]/[1-\gamma^2])$ and ellipticity $E(= 1-\gamma)$ with dispersion σ_T and σ_E.

For a given set of parameters (T,E,σ_T,σ_E), we numerically generate distributions for β and γ. Then, a random viewing angle (θ,ϕ) is assigned to each of the elements of the distribution (100,000 in our case) such that with Equation (3) the projected axis ratio distribution can be generated. This distribution corresponds to the probability distribution $p(q_{model})$.

For nearly round ($q \sim 1$) galaxies, random noise will always cause the measured q to be an underestimate as the position angle of the long axis becomes ill-determined. This affects the projected axis-ratio distribution as described by Rix & Zaritsky (1995) (Equation (C5)):

$$P_e(\epsilon, \epsilon_e, \Delta\epsilon) = \frac{\epsilon}{\Delta\epsilon^2} I_o\left(\frac{\epsilon\epsilon_e}{\Delta\epsilon^2}\right)\exp\left(-\frac{\epsilon^2 + \epsilon_e^2}{2\Delta\epsilon^2}\right), \quad (4)$$

where $\epsilon(= 1-q)$ is the measured ellipticity, ϵ_e is the expected ellipticity, $\Delta\epsilon$ is the measured error, and P_e is the expected ellipticity distribution. We numerically implement the difference between ϵ and ϵ_e to correct the generated probability distribution $p(q_{model})$. We adopt fixed values $\Delta\epsilon = \Delta q$ for each of the data sets used here: 0.03 and 0.05 for the low- and high-z data sets from H12, and 0.04 for the CANDELS data set.

The total likelihood L for a measured set projected axis ratios q_{data} and a given set of model parameters T, E, σ_T, and σ_E is given by $L = \Sigma_{q_{data}} \log p(q_{data}|q_{model})$, where p has a minimum value of 0.01.

L is computed for a grid of model parameters, chosen in various ways for the different approaches explored below, such that the maximum likelihood model can be located in the grid and the best-fitting model is identified.

In order to obtain uncertainty estimates on the best-fitting model parameters, we bootstrap the observed data (q_{data}), also perturbing q_{data} by the measurement uncertainty and perturbing the redshift and stellar mass estimates as described in Section 3.

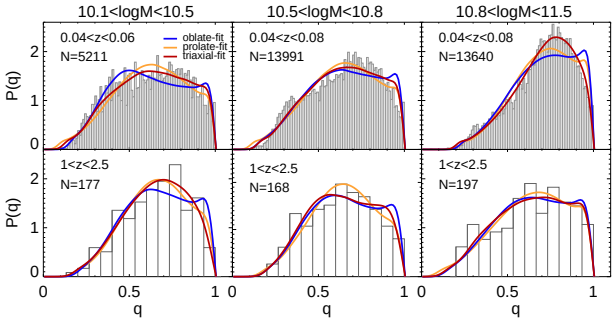

FIG. 7.— Histograms show observed distributions of projected axis ratios for present-day early-type galaxies from SDSS (upper row) and at $1 < z < 2.5$ from CANDELS (bottom row), each in three mass bins. The colored lines represent the best-fitting, single-component models with Gaussian distributions for intrinsic axis ratios, with the oblate model in blue, the prolate model in orange, and the triaxial model in red. See Section 5.1.1 for details. The mean and dispersion of the best-fitting Gaussians are listed in Table 2.

5.1. *Application*

5.1.1. *Single-component Model for the Intrinsic Shape*

For each of the SDSS (vdW09), COSMOS/GEMS (H12), and CANDELS data sets we search for the best-fitting triaxial model as described above on a grid spaced as (ΔT, $\Delta\sigma_T$, ΔE, $\Delta\sigma_E$)=(0.04, 0.04, 0.01, 0.01). We separately consider the two special cases: oblate, with $T = 0$ and $\sigma_T = 0$; and prolate, with $T = 1$ and $\sigma_T = 0$. As before, the samples are analyzed in bins of stellar mass and redshift. The results are given in Table 2 and a subset are shown in Figure 7. For each best-fitting model we estimate the goodness-of-fit by computing the K-S and M-W probabilities that the observed q_{data} represent a population of galaxies with a projected axis ratio distribution q_{model}. Note that our fitting method does not aim to maximize the probabilities given by these goodness-of-fit indicators.

As noted by H12, the axis ratio distribution of present-day early-type galaxies cannot generally be accurately described by a single-component model with Gaussian distributions for the intrinsic parameters. The one exception is that massive early-type galaxies ($\log(M_*/M_\odot) > 10.8$) quite closely resemble a single, highly triaxial population ($T = 0.6$). At all redshifts up to $z = 2.5$ no prolate model fits the data, while an oblate model cannot be ruled out. The oblate model fitting results reflect

TABLE 2
Single-component Fitting Results

Model	Mass($\log(M_*/M_\odot)$)	Redshift(z)	T [a]	σ_T	E [b]	σ_E	P_{KS} [c]	P_{MW}
Single oblate model								
Oblate	10.8-11.5	0.04-0.08 (SDSS)	0	0	0.48 ± 0.01 [d]	0.18 ± 0.01	*0.00* [e]	*0.01*
Oblate	10.5-10.8	0.04-0.08 (SDSS)	0	0	0.61 ± 0.00	0.18 ± 0.00	*0.00*	*0.01*
Oblate	10.1-10.5	0.04-0.06 (SDSS)	0	0	0.66 ± 0.01	0.13 ± 0.01	*0.00*	0.16
Oblate	10.8-11.5	0.6-0.8 (H12)	0	0	0.46 ± 0.03	0.17 ± 0.03	0.21	0.20
Oblate	10.5-10.8	0.6-0.8 (H12)	0	0	0.58 ± 0.04	0.17 ± 0.04	0.24	0.46
Oblate	10.1-10.5	0.6-0.8 (H12)	0	0	0.58 ± 0.03	0.14 ± 0.03	0.12	0.13
Oblate	10.8-11.5	1-2.5	0	0	0.61 ± 0.03	0.18 ± 0.03	0.99	0.45
Oblate	10.5-10.8	1-2.5	0	0	0.59 ± 0.04	0.14 ± 0.03	0.69	0.26
Oblate	10.1-10.5	1-2.5	0	0	0.56 ± 0.03	0.15 ± 0.03	0.41	0.34
Single prolate model								
Prolate	10.8-11.5	0.04-0.08 (SDSS)	1	0	0.37 ± 0.00	0.18 ± 0.00	*0.00*	0.34
Prolate	10.5-10.8	0.04-0.08 (SDSS)	1	0	0.45 ± 0.00	0.20 ± 0.01	*0.00*	0.07
Prolate	10.1-10.5	0.04-0.06 (SDSS)	1	0	0.47 ± 0.00	0.20 ± 0.00	*0.00*	0.35
Prolate	10.8-11.5	0.6-0.8 (H12)	1	0	0.36 ± 0.02	0.17 ± 0.02	0.70	0.26
Prolate	10.5-10.8	0.6-0.8 (H12)	1	0	0.42 ± 0.03	0.20 ± 0.02	0.29	0.35
Prolate	10.1-10.5	0.6-0.8 (H12)	1	0	0.45 ± 0.02	0.17 ± 0.02	0.24	0.41
Prolate	10.8-11.5	1-2.5	1	0	0.44 ± 0.03	0.21 ± 0.02	0.90	0.48
Prolate	10.5-10.8	1-2.5	1	0	0.45 ± 0.02	0.17 ± 0.02	0.55	0.37
Prolate	10.1-10.5	1-2.5	1	0	0.43 ± 0.02	0.17 ± 0.02	0.61	0.47
Single triaxial model								
Triaxial	10.8-11.5	0.04-0.08 (SDSS)	$0.60^{+0.00}_{-0.08}$	$0.16^{+0.00}_{-0.12}$	$0.45^{+0.02}_{-0.00}$	$0.23^{+0.00}_{-0.01}$	*0.03*	0.15
Triaxial	10.5-10.8	0.04-0.08 (SDSS)	$0.92^{+0.00}_{-0.92}$	$0.00^{+0.66}_{-0.00}$	$0.47^{+0.16}_{-0.00}$	$0.24^{+0.00}_{-0.06}$	*0.00*	0.12
Triaxial	10.1-10.5	0.04-0.06 (SDSS)	$0.92^{+0.02}_{-0.92}$	$0.00^{+0.24}_{-0.00}$	$0.50^{+0.17}_{-0.00}$	$0.26^{+0.00}_{-0.11}$	*0.03*	0.13
Triaxial	10.8-11.5	0.6-0.8 (H12)	$0.76^{+0.00}_{-0.62}$	$0.92^{+0.00}_{-0.92}$	$0.44^{+0.06}_{-0.05}$	$0.20^{+0.05}_{-0.04}$	0.82	0.34
Triaxial	10.5-10.8	0.6-0.8 (H12)	$0.92^{+0.00}_{-0.72}$	$0.00^{+0.06}_{-0.00}$	$0.43^{+0.20}_{-0.00}$	$0.25^{+0.09}_{-0.06}$	0.39	0.18
Triaxial	10.1-10.5	0.6-0.8 (H12)	$0.92^{+0.04}_{-0.88}$	$0.00^{+0.28}_{-0.00}$	$0.47^{+0.18}_{-0.00}$	$0.21^{+0.04}_{-0.09}$	0.40	0.26
Triaxial	10.5-10.8	1-2.5	$0.00^{+0.72}_{-0.00}$	$0.20^{+0.08}_{-0.20}$	$0.61^{+0.05}_{-0.10}$	$0.13^{+0.06}_{-0.05}$	0.53	0.38
Triaxial	10.8-11.5	1-2.5	$0.92^{+0.04}_{-0.82}$	$0.00^{+0.04}_{-0.00}$	$0.47^{+0.17}_{-0.03}$	$0.26^{+0.02}_{-0.11}$	0.75	0.33
Triaxial	10.1-10.5	1-2.5	$0.00^{+0.80}_{-0.00}$	$0.52^{+0.00}_{-0.52}$	$0.56^{+0.05}_{-0.07}$	$0.17^{+0.07}_{-0.03}$	0.70	0.47

[a] T is the mean triaxiality parameter, with standard deviation σ_T; these are set to 0 or 1 for the oblate and prolate models.
[b] E and σ_E are the ellipticity (1 minus the intrinsic short-long axis ratio) and its standard deviation.
[c] The final two columns list the K-S and M-W probabilities that the observed and best-fitting model projected axis ratio distributions are indistinguishable, for a randomly drawn realization of the model distribution with the same number of objects as the observed samples. These serve as a crude goodness-of-fit test.
[d] Uncertainties are obtained from bootstrapping.
[e] The asterisks (*) represent the significant probability is smaller than 5%. It implies that the distributions are distinguishable.

the previously mentioned evolution in the median axis ratio: the intrinsic ellipticity for the most massive galaxies increases from $E = 0.48$ at $z < 0.1$ to $E = 0.61$ at $z > 1$, while it decreases from $E = 0.66$ to $E = 0.56$ for galaxies in the mass range $10.1 < \log(M_*/M_\odot) < 10.5$.

5.1.2. *Two-component Model for the Intrinsic Shapes*

Because the single-component models with Gaussian distributions for the intrinsic shape parameters cannot reproduce the shape distribution of the low-redshift sample, we now explore a different approach. As shown most recently by H12, a two-component model can accurately describe the axis-ratio distribution of present-day early-type galaxies over a large range in mass. One of these components is triaxial, precisely of the form used above; the other component is oblate, with a normally distributed intrinsic axis ratio, with mean b and standard deviation σ_b. Thus, we now have six parameters that describe the intrinsic shape distribution; the seventh free parameter is the fraction assigned to the oblate component (f_{ob}). The spacing of the grid we now use to search for the best-fitting model is (Δf_{ob}, ΔT, $\Delta\sigma_T$, ΔE, $\Delta\sigma_E$, Δb, $\Delta\sigma_b$)=(0.04, 0.04, 0.02, 0.01, 0.01, 0.01, 0.01, 0.01).

The two-component approach results in a very good description of the observed axis ratio distributions of present-day galaxies (see Table 3 and Figure 8). The goodness-of-fit indications from the K-S and M-W statistical tests suggest that the best-fitting models provide a realistic view of the intrinsic shape distribution. Over the entire galaxy mass range, a highly triaxial ($T \sim 0.6$), yet flattened ($E \sim 0.45$), component combined with an even flatter ($b \sim 0.3$) oblate component provides a good description of the data, with little variation in these shape parameters with galaxy mass. The parameter that captures the strong mass-dependence in galaxy structure is f_{ob}, the fraction assigned to the second, oblate component: it rises from $f_{ob} = 0.20 \pm 0.02$ at high mass to $f_{ob} = 0.72 \pm 0.06$ at low mass.

These results are very similar to those presented by H12 – small differences occur due the choice of different stellar mass bins as well as a different implementation of the intrinsic variation in the shape parameters – the σ parameters – in generating the probability distributions $p(q_{model})$.

The high-redshift samples are too small to be treated with seven independent free parameters. However, given the success of the two-component model in describing the shape distribution of present-day early-type galaxies, we can use our superior knowledge of the low-redshift

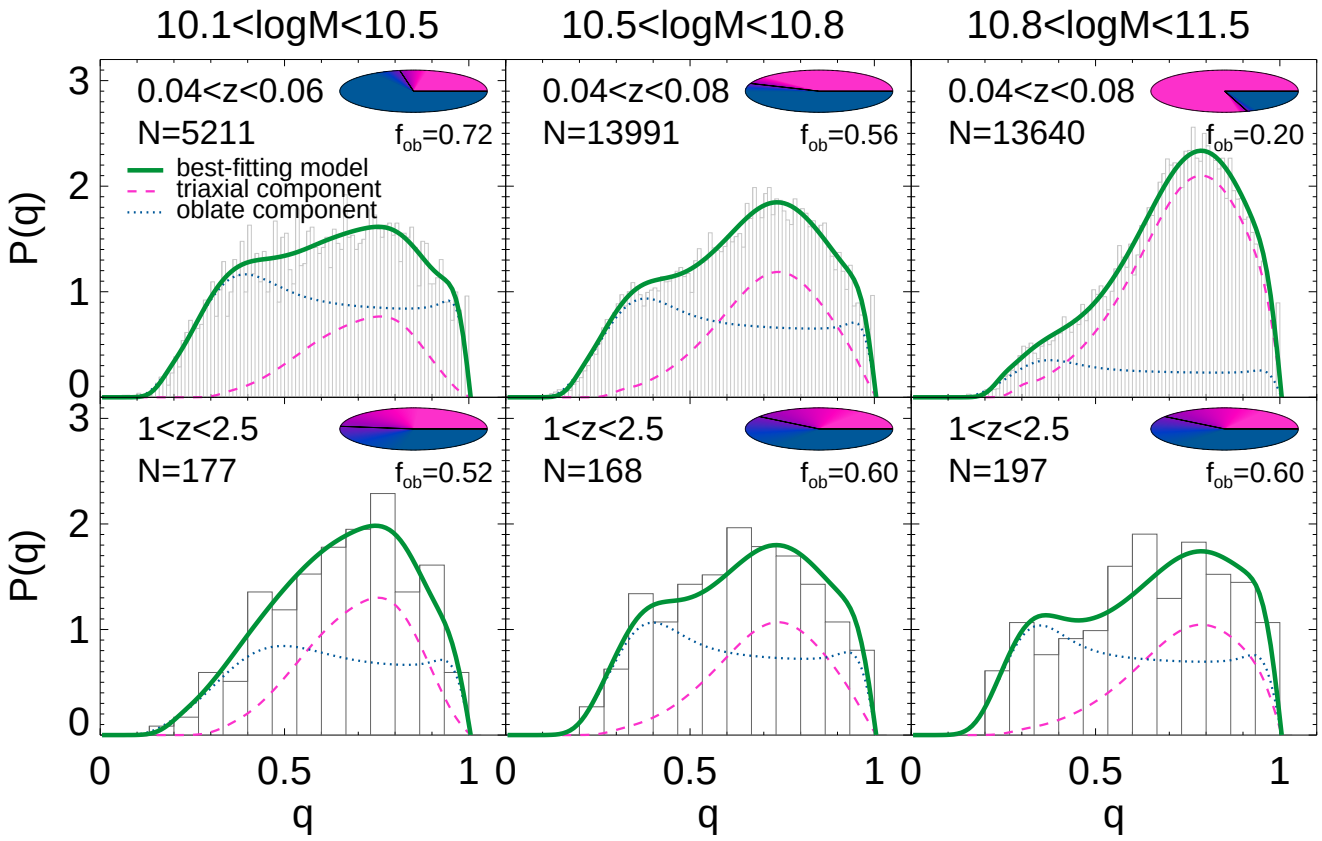

FIG. 8.— Histograms show observed distributions of projected axis ratios for present-day early-type galaxies from SDSS (upper row) and at $1 < z < 2.5$ from CANDELS (bottom row), each in three mass bins. The green lines represent the best-fitting, two-component models with Gaussian distributions for intrinsic axis ratios as described in Section 5.1.2. The dashed pink lines respresent the triaxial component; the dotted blue lines represent the oblate component. The parameters characterizing the Gaussians are given in Tables 3 and 4. The small pie charts represent f_{ob}, the oblate fraction, and its uncertainty. For the CANDELS sample, the triaxial components are assumed to be identical to the best-fitting triaxial components found for the SDSS sample in the same mass bin. The strong dependence of the oblate fraction on galaxy mass is much weakened at $z > 1$. The most striking feature is the large fraction of oblate, that is, disk-like galaxies in the high-mass bin.

TABLE 3
DOUBLE-COMPONENT FITTING RESULTS FOR $z = 0$

Mass	redshift(z)	f_{ob} [a]	b [b]	σ_b	T [c]	σ_T	E [d]	σ_E	P_{KS} [e]	P_{MW}
10.8-11.5	0.04-0.08 (SDSS)	0.20 ± 0.02 [f]	0.29 ± 0.02	0.07 ± 0.01	0.64 ± 0.06	0.08 ± 0.05	0.41 ± 0.02	0.19 ± 0.02	0.26	0.46
10.5-10.8	0.04-0.08 (SDSS)	0.56 ± 0.06	0.28 ± 0.01	0.08 ± 0.01	0.68 ± 0.12	0.08 ± 0.06	0.45 ± 0.02	0.16 ± 0.03	0.29	0.19
10.1-10.5	0.04-0.06 (SDSS)	0.72 ± 0.06	0.28 ± 0.01	0.09 ± 0.01	0.48 ± 0.08	0.08 ± 0.06	0.49 ± 0.02	0.12 ± 0.02	0.84	0.28

[a] $f_{\rm ob}$ is the fraction of the oblate component.
[b] b the intrinsic axis ratio of the oblate component and σ_b its standard deviation.
[c] T is the mean triaxiality parameter, with standard deviation $\sigma_{\rm T}$; these are set to 0 or 1 for the oblate and prolate models.
[d] E and σ_E are the ellipticity (1 minus the intrinsic short-long axis ratio) and its standard deviation.
[e] The final two columns list the K-S and M-W probabilities that the observed and best-fitting model projected axis ratio distributions are indistinguishable, for a randomly drawn realization of the model distribution with the same number of objects as the observed samples. These serve as a crude goodness-of-fit test.
[f] Uncertainties are obtained from bootstrapping.

population to inform the model for the high-redshift population. Because each of the two components are very similar across the mass range explored here for the low-redshift sample, we assume that the same components can be used as an appropriate model to describe the higher-redshift observations. First, we use the best-fitting triaxial component for each of the three mass bins, with fixed intrinsic shape distributions, but let the oblate component vary arbitrarily. That is, the parameters b, σ_b, and f_{ob} are allowed to vary, while the others are kept fixed. The results are shown in Table 4 and Figure 8.

For the COSMOS+GEMS and combined ($1 < z < 2.5$) CANDELS samples we find that all evolution with redshift can be accounted for by evolution in f_{ob}; no significant changes in b (or σ_b) are seen. For the highest-mass galaxies ($10.8 < \log(M_*/M_\odot) < 11.5$) f_{ob} is seen to rise at $z > 1$, from $f_{ob} \sim 0.2$ at $z < 1$ to $f_{ob} = 0.60 \pm 0.24$. The large uncertainty is due to the degeneracy between

TABLE 4
Double-component Fitting Results for $z = 0.6 - 2.5$

Mass	Redshift(z)	Oblate Parameters Free [a]					Oblate Fraction Free [b]		
		f_{ob} [c]	b [d]	σ_b	P_{KS} [e]	P_{MW}	f_{ob}	P_{KS}	P_{MW}
10.8-11.5	0.6-0.8 (H12)	0.16 ± 0.18 [f]	0.33 ± 0.10	0.05 ± 0.08	0.70	0.36	0.12 ± 0.06	0.43	0.26
10.5-10.8	0.6-0.8 (H12)	0.48 ± 0.23	0.28 ± 0.07	0.05 ± 0.06	0.21	0.24	0.49 ± 0.08	0.22	0.24
10.1-10.5	0.6-0.8 (H12)	0.56 ± 0.12	0.32 ± 0.03	0.06 ± 0.04	0.87	0.36	0.51 ± 0.08	0.67	0.38
10.8-11.5	1-2.5	0.60 ± 0.24	0.27 ± 0.07	0.06 ± 0.05	0.71	0.49	0.59 ± 0.10	0.54	0.40
10.5-10.8	1-2.5	0.60 ± 0.25	0.31 ± 0.07	0.07 ± 0.03	0.87	0.37	0.53 ± 0.14	0.61	0.33
10.1-10.5	1-2.5	0.52 ± 0.24	0.34 ± 0.10	0.12 ± 0.06	0.69	0.46	0.38 ± 0.11	0.12	0.16
Redshift Bins of CANDELS									
10.8-11.5	0.6-0.8	1.00 ± 0.31	0.52 ± 0.13	0.25 ± 0.10	0.96	0.44	0.35 ± 0.20	0.25	0.29
10.8-11.5	0.8-1.3	0.84 ± 0.21	0.29 ± 0.05	0.06 ± 0.05	0.99	0.50	0.81 ± 0.20	0.97	0.44
10.8-11.5	1.3-1.8	0.48 ± 0.28	0.22 ± 0.08	0.05 ± 0.07	0.89	0.46	0.59 ± 0.16	0.73	0.48
10.8-11.5	1.8-2.5	1.00 ± 0.27	0.41 ± 0.09	0.20 ± 0.07	0.97	0.44	0.51 ± 0.21	0.94	0.45
10.5-10.8	0.6-0.8	0.36 ± 0.31	0.27 ± 0.10	0.05 ± 0.09	0.92	0.46	0.42 ± 0.24	0.89	0.49
10.5-10.8	0.8-1.3	1.00 ± 0.28	0.40 ± 0.07	0.16 ± 0.07	0.99	0.49	0.53 ± 0.27	0.87	0.48
10.5-10.8	1.3-1.8	0.64 ± 0.31	0.30 ± 0.10	0.05 ± 0.08	0.67	0.30	0.63 ± 0.24	0.66	0.31
10.5-10.8	1.8-2.5	0.56 ± 0.32	0.29 ± 0.09	0.05 ± 0.03	0.93	0.39	0.55 ± 0.28	0.92	0.38
10.1-10.5	0.6-0.8	0.56 ± 0.28	0.26 ± 0.09	0.05 ± 0.08	0.63	0.32	0.57 ± 0.19	0.68	0.37
10.1-10.5	0.8-1.3	0.84 ± 0.26	0.46 ± 0.08	0.17 ± 0.10	0.97	0.45	0.31 ± 0.18	0.41	0.28
10.1-10.5	1.3-1.8	0.44 ± 0.36	0.23 ± 0.12	0.19 ± 0.10	0.37	0.19	0.47 ± 0.20	0.94	0.42
10.1-10.5	1.8-2.5	0.80 ± 0.28	0.31 ± 0.10	0.05 ± 0.06	0.47	0.28	0.71 ± 0.35	0.82	0.46

[a]Fix triaxial component in the same stellar mass bins as local galaxies.
[b]Fix other parameters in the same stellar mass bins as local galaxies.
[c]$f_{\rm ob}$ is the fraction of the oblate component.
[d]b the intrinsic axis ratio of the oblate component and σ_b its standard deviation.
[e]The final two columns list the K-S and M-W probabilities that the observed and best-fitting model projected axis ratio distributions are indistinguishable, for a randomly drawn realization of the model distribution with the same number of objects as the observed samples. These serve as a crude goodness-of-fit test.
[f]Uncertainties are obtained from bootstrapping.

b and f_{ob}: evolution in the average shape can either be accommodated by a change in the average shape of the galaxies represented by the oblate component, or by a change in the fraction of oblate galaxies. The unsubstantial changes in b (σ_b) with mass and redshift motivate us to implement a second restriction to our model: we now keep all intrinsic shape parameters at the values found for the low-z SDSS sample, and only allow f_{ob} to vary.

This restriction seems justified by the results from the goodness-of-fit tests: the predicted distribution from the best-fitting models, even with only a single free parameter (f_{ob}), do not significantly differ from the observed distributions according the the the K-S and M-W tests. The results are also shown in Table 4 and Figure 9. We now find that the oblate fraction for the massive galaxies increases from 0.20 ± 0.02 at $z < 0.1$ to 0.59 ± 0.10 at $z > 1$, a highly significant (4σ) change. For galaxies in our middle mass bin ($10.5 < \log(M_*/M_\odot) < 11.8$), f_{ob} does not change with redshift and stays at $\sim 0.5 - 0.6$, whereas, remarkably, f_{ob} significantly declines from 0.72 ± 0.06 to 0.38 ± 0.11 for low-mass galaxies ($10.1 < \log(M_*/M_\odot) < 10.5$). The latter was already reflected by the increased median axis ratio with redshift (see Section 3).

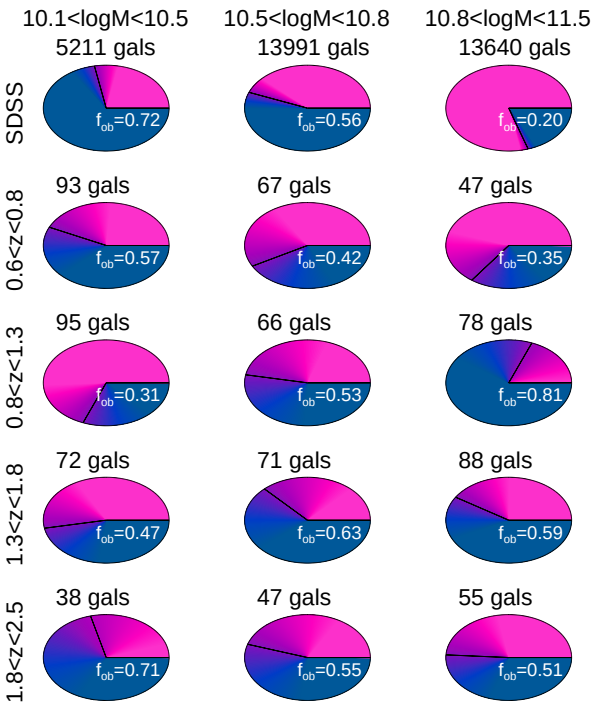

Fig. 9.— The evolution of the oblate fraction of early-type galaxies in different mass bins. Compared to the results shown in Figure 8, the redshift bins at $z > 1$ are now narrower, as indicated, and the intrinsic shape distributions of both the oblate and the triaxial component are kept fixed at the values found for the present-day SDSS sample. The values of f_{ob} and their uncertainties are given in Table 4.

6. DISCUSSION

L^* early-type galaxies ($M_* \sim 10^{11} M_\odot$) in the present-day universe possess a wide range of intrinsic shapes: there is no single oblate, prolate, or triaxial shape that, viewed from any number of random viewing angles, can account for their projected axis ratio distribution (e.g., Lambas et al. 1992; Tremblay & Merritt 1996). We implemented two methods to describe and model this distribution. First, we showed that a single family of oblate or prolate structures with broadly distributed intrinsic axis

ratios accurately captures the observed projected distribution (Section 4 and Figure 6). Second, we showed that a combination of triaxial and oblate structures, with normally distributed intrinsic shapes, works equally well. This second approach is attractive as the distinction of two components corresponds to the kinematical distinction between 'fast rotators' and 'slow rotators' (e.g., Emsellem et al. 2011). Figure 8 shows that a triaxial component combined with a thinner, oblate component provides a good description over a large range of galaxy masses. The strong dependence of galaxy structure on stellar mass is driven by the variation in the relative abundances of triaxial and oblate objects. We now discuss the evolution of the intrinsic shape distribution of early-type galaxies, based on our analysis presented in Section 3, 4, and 5.

6.1. *Increased Incidence of Disk-Like, Massive Early-type Galaxies at $z > 1$*

The cumulative distributions of projected axis ratios of L^* early-type galaxies at $z > 1$ and at the present-day show that these were on average flatter in the past (Section 3; Figure 5). Our parameterized modeling approach presented Section 5.1.2 interprets this as a change in the fraction of the oblate component, from 0.20 ± 0.02 at $z < 0.1$ to 0.59 ± 0.10 at $z > 1$.

Because the $z > 1$ sample is too small to directly distinguish what structural family the galaxies belong to, we consider independent evidence for our interpretation that the $z > 1$ population largely consists of flat, oblate objects. At the present day, flatness is associated with rotation (e.g., van den Bosch et al. 2008; Emsellem et al. 2011), but so far such kinematic evidence has not been extended beyond $z \sim 1$ (van der Wel & van der Marel 2008). The best direct evidence for our interpretation that flat galaxies in our sample are indeed disk-like in structure is that the stellar surface mass density (middle panel of Figure 10) and the surface brightness (bottom panel of Figure 10) are larger for galaxies with small projected axis ratios. This is expected in case the flat galaxies are edge-on and oblate, but not if they are edge-on and prolate. In the latter case, the flattest galaxies should have the smallest surface brightness. We note that these considerations are only valid for transparent, that is, dust-poor, stellar systems. This assumption is supported by the observation that the rest-frame $V - J$ color does not significantly change with projected axis ratio, implying little variation in dust attenuation with inclination and, thus, a low dust content. The lack of star formation activity in these objects combined with their low dust content indicate that our sample consists of galaxies with smooth light profiles, and is therefore comparable to a morphologically classified sample of early-type galaxies based on visual inspection of images.

Further direct evidence of prominent disks in high-redshift early-type galaxies comes from two-dimensional bulge-disk decompositions (Stockton et al. 2006, 2008; McGrath et al. 2008; van der Wel et al. 2011; Bruce et al. 2012)

Based on these independent lines of evidence, we conclude that at $z > 1$ a substantially larger fraction of L^* early-type galaxies are disk-like than at $z < 1$. This evolution in structure coincides with evolution in size (e.g., Zirm et al. 2007; Toft et al. 2007; van Dokkum et al. 2008; van der Wel et al. 2008; Newman et al. 2012). Van der Wel et al. (2013a, in preparation) showed that the number density of small ($\lesssim$ 2kpc) early-type galaxies dramatically decreases between $z \sim 2$ and the present day (also see Cassata et al. 2011, 2013). These early types are, as we have shown here, commonly disk-like, such that we may conclude that individual galaxies evolve from small and disk-like at $z \sim 2$ to large and round at $z \sim 0$. The evolution of size and internal structure could be driven by a single process, and merging is usually considered to be the most plausible process (e.g., Robaina et al. 2010; Man et al. 2012; Newman et al. 2012). Major merging and more smooth

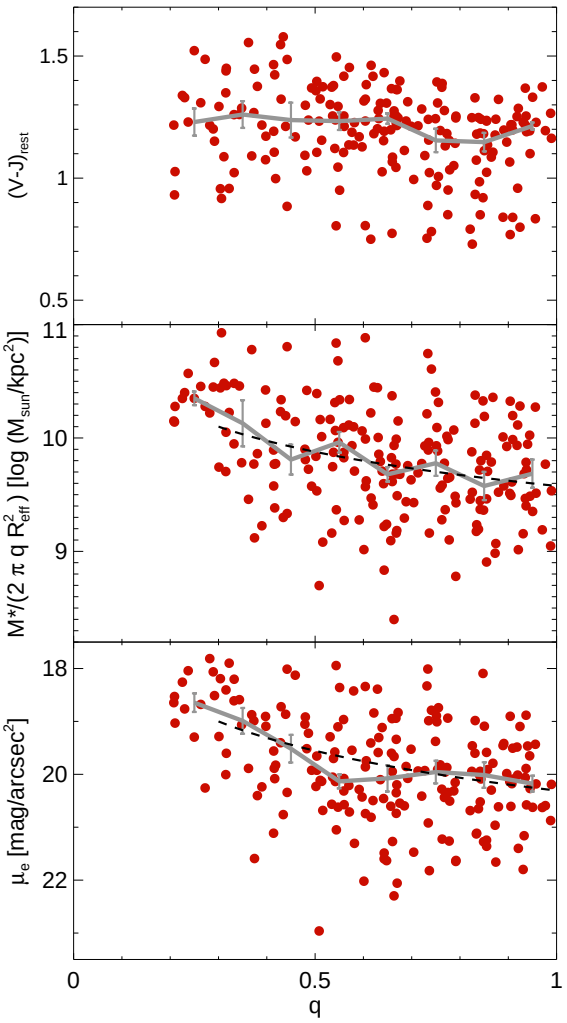

FIG. 10.— The projected axis ratio vs. rest-frame $V - J$ color, mass surface density, and surface brightness for the early-type galaxies selected from CANDELS at redshifts $1 < z < 2.5$ and more massive than $\log(M_*/M_\odot) > 10.8$. The gray lines with error bars from bootstrapping represent running medians. The lack of a trend in the top panel suggests that these galaxies contain little or no dust; otherwise, galaxies with small axis ratios, that is, those viewed edge-on, would be expected to have redder colors. The increased surface mass density and surface brightness of the small-axis ratio galaxies (bottom two panels) suggest that these galaxies are oblate rather than prolate; the dashed black lines are the expected projected surface brightness and density for an oblate model, with intrinsic axis ratio $E = 0.61$, which is the best-fitting value from the single-component model for this sample (Table 2).

growth in mass through accretion and disruption of satellites can account for the disappearance of prominent disks in L^* early types at $z \sim 2$, and the observation that the most massive galaxies in the present-day universe do not host disks (vdW09).

In addition to the growth of individual galaxies, evolution in the population is driven by the strong increase in the number density of early-type galaxies between $z \sim 2$ and the present (e.g., Bell et al. 2004; Faber et al. 2007; Brammer et al. 2011). From $z = 2$ to $z = 1$ the fraction of triaxial galaxies increases, but this cannot be the result of the formation of 'new' early-type galaxies in the form of triaxial systems from already-formed early-type galaxies. The absolute number densities of oblate and triaxial systems both increase over that time span, and we suggest that all 'new' early types start out as compact and disk-like and subsequently evolve into larger, more triaxial systems (e.g., Naab et al. 2009; Oser et al. 2012). This suggestion is motivated by the notion that the immediate progenitors of 'new' early-type galaxies will be gas rich and star-forming, creating suitable circumstances for the formation of disks (see below), and by the notion that it is implausible that round, triaxial systems evolve into disk-like systems in the absence of star formation. At $z < 1$ a natural balance is established between the addition of 'new', disk-like early types and the gradual formation of triaxial systems, resulting in an almost unchanging, but strongly varied mix of intrinsic structures, as discussed by H12.

In the scenario described above, galaxies in which star formation is truncated retain the disk-like structure of their presumed, star-forming progenitors. A full discussion of the transition process is beyond the scope of this paper, but it is important to point out that while newly formed early-type galaxies retain disk-like properties, their light (and stellar mass) distributions are more centrally concentrated than those of equally massive star-forming galaxies (e.g., Toft et al. 2009; Wuyts et al. 2011; Bell et al. 2012). This implies that a substantial increase in the central stellar density occurs before or at the time of transition. A centrally concentrated starburst fueled by a gas-rich merger is one possible mechanism to produce bulge-like bodies (e.g., Khochfar & Silk 2006). More recently, violent disk instabilities in a gas-rich galaxy have been argued to produce clumps that may migrate to the center on a short time scale, quickly creating a dense stellar body (Dekel et al. 2009; Ceverino et al. 2010; Guo et al. 2012). Whether the gas content of the resulting, dense, disk-like, but non-star-forming, galaxy has been heated and removed (e.g., Hopkins et al. 2008) or merely stabilized (e.g., Martig et al. 2009; Ceverino et al. 2012) is still debated.

6.2. *Decreased Incidence of Disk-like, Low-mass Early-type Galaxies at $z > 1$*

Sub-L^* early-type galaxies ($M_* \sim 10^{10} M_\odot$) in the local universe are most often oblate and disk-like. The comparison with the cumulative axis ratio distributions of such objects at $z > 1$ tells us that these were less disk-like (see Figure 5). This may appear to be at odds with the results discussed above, that is, that massive early types were more disk-like at $z > 1$.

Our interpretation of this 3σ effect remains largely speculative. Low-mass early-type galaxies in the present day can be surmised to be disk-like for the simple reason that their star-forming progenitors are also disk-like. Star formation may stop either due to some internal process or due to environmental effects such as ram-pressure stripping. In the latter case the structure of the stellar disk will remain intact, leading to a very flat early-type galaxy. At $z \sim 2$ the fraction of satellite galaxies in this mass range is predicted to be negligible, whereas among the present-day population satellite galaxies make up $30\% - 40\%$ of the total (e.g., van den Bosch et al. 2008). Indeed, the axis ratio distributions of present-day centrals and satellites are significantly different (van der Wel et al. 2010), but even the present-day centrals are not as round as their $z > 1$ counterparts (also see Vulcani et al. 2011),. We suggest that the low-mass early-type galaxies at $z > 1$ are not very disk-like, simply because their star-forming progenitors were not disk-like at that epoch: van der Wel et al. (2013b, in preparation) showed that low-mass ($M_* < M_\odot^{10}$) star-forming galaxies at $z > 1$ had not yet attained stable, rotating structures, like they have at later epochs. Whether this is related remains to be seen and hinges on our general lack of understanding of how star-forming galaxies are transformed into passive, early-type galaxies.

7. SUMMARY

Projected axis ratio measurements from HST/WFC3 F160W imaging from CANDELS of 880 early-type galaxies at redshifts $1 < z < 2.5$, complete down to a stellar mass of $\log(M_*/M_\odot) = 10$ over the whole redshift range, are used to reconstruct and model their intrinsic shapes. The sample is selected by low star-formation activity on the basis of $U - V$ and $V - J$ rest-frame colors (see Figure 2, and we demonstrate that these galaxies are dust-poor and transparent: those with flat projected shapes have the same colors as those with round shapes (see Figure 10, top panel). In addition, the increased surface mass densities and surface brightness of flat galaxies (Figure 10, bottom two panels) suggest that flattening is associated with a disk-like internal structure; prolate galaxies would have lower surface densities when viewed edge-on. Therefore, we conclude that our sample consists of genuine early types, comparable to samples based on visual morphological classification. We compare the shape distribution of this sample with the shape distribution of early-type at low redshift ($0.04 < z < 0.08$) selected in a similar manner from the SDSS.

Similar to their present-day counterparts, the $z > 1$ early-type galaxies show a large variety in intrinsic shape; even at a fixed mass, the projected axis ratio distributions cannot be explained by random projection of a set of galaxies with very similar intrinsic shapes. We demonstrated this in two ways by assuming that all galaxies are oblate (or prolate): first, an analytical approximation to deproject the observed axis ratio distributions implies that a very broad range in intrinsic shapes is required (Section 4 and Figure 6); second, we show that randomly projecting a set of objects with a Gaussian distribution of intrinsic axis ratios cannot match the observed, projected shape distribution (Section 5.1.1 and Figure 7).

As was demonstrated for present-day early-type galaxies and up to $z \sim 1$, a two-population model can ac-

curately describe the projected axis ratio distributions. We now extend this to $z = 2.5$. This model, inferred from fitting the axis ratio distribution of the low-redshift sample (Section5.1.2 and Figure 8), consists of a triaxial, fairly round population combined with a flat ($c/a \sim 0.3$) oblate population. For present-day early-type galaxies the oblate fraction strongly depends on galaxy mass, but at $z > 1$ this trend is not seen over the stellar mass range explored here ($10 < \log(M_*/M_\odot) < 11.3$). This is mostly the result of strong evolution in the oblate fraction among high-mass early-type galaxies: for galaxies with mass $\log(M_*/M_\odot) > 10.8$ the oblate fraction increases from 0.20 ± 0.02 at the present day to 0.59 ± 0.10 at $1 < z < 2.5$. Conversely, we find that the oblate fraction decreases with redshift for low-mass early-type galaxies ($\log(M_*/M_\odot) < 10.5$), from 0.72 ± 0.06 to 0.38 ± 0.11. These results are based on the assumption that the intrinsic shapes of the triaxial and oblate population do not evolve with redshift. We refer to Section 5.1.2 for a justification of this assumption and a demonstration that our results and interpretation do not depend on it.

The decreased prevalence of disk-like systems and larger galaxy sizes at lower redshifts point to a scenario in which classical elliptical galaxies gradually emerge over time through merging and the accretion of satellites, at the expense of the destruction of pre-existing disks. Definitive evidence for the disk-like structure of massive early-type galaxies at $z \sim 2$ should eventually be provided by kinematic evidence for rotation in the stellar body. We speculate that the decreased incidence of disks at early cosmic times among low-mass early-type galaxies can be attributed to two factors: low-mass, star-forming progenitors at $z > 1$ were not settled into stable disks to the same degree as at later cosmic times, and the stripping of gas from satellite galaxies is an increasingly important process at lower redshifts. We refer to Section 6.2 for a discussion.

A joint analysis of shapes, sizes, and Sérsic indices for late- and early-type galaxies, will provide further insight into the intrinsic structure of high-redshift galaxies, and allow for more constrained deprojection and model construction approaches. Further improvements will be provided by the extension of the analysis to the full CANDELS data set, drawing samples from all five fields instead of the two fields used here; at the moment we are still limited by small number statistics at $z \sim 2$ and above.

We thank the anonymous referee for helpful comments, and Steve Willner and Matthew Ashby for useful suggestions. This work is based on observations taken by the CANDELS Multi-Cycle Treasury Program with the NASA/ESA HST, which is operated by the Association of Universities for Research in Astronomy, Inc., under NASA contract NAS5-26555. Y.-Y. C. was funded by the IMPRS for Astronomy & Cosmic Physics at the University of Heidelberg and the Marie Curie Initial Training Network ELIXIR of the European Commission under contract PITN-GA-2008-214227.

REFERENCES

Ashby, M. L. N., Willner, S. P., Fazio, G. G., et al. 2013, ApJ, 769, 80
Bell, E. F. 2008, ApJ, 682, 355
Bell, E. F., et al. 2004, ApJ, 608, 752
—. 2012, ApJ, 753, 167
Binney, J. 1978, MNRAS, 183, 501
—. 1985, MNRAS, 212, 767
Brammer, G. B., van Dokkum, P. G., & Coppi, P. 2008, ApJ, 686, 1503
Brammer, G. B., et al. 2011, ApJ, 739, 24
Bruce, V. A., et al. 2012, MNRAS, 427, 1666
Bruzual, G., & Charlot, S. 2003, MNRAS, 344, 1000
Buitrago, F., Trujillo, I., Conselice, C. J., & Häußler, B. 2013, MNRAS, 428, 1460
Cassata, P., et al. 2011, ApJ, 743, 96
Cassata, P., et al. 2013, arXiv:1303.2689
Ceverino, D., Dekel, A., & Bournaud, F. 2010, MNRAS, 404, 2151
Ceverino, D., Dekel, A., Mandelker, N., Bournaud, F., Burkert, A., Genzel, R., & Primack, J. 2012, MNRAS, 420, 3490
Chabrier, G. 2003, PASP, 115, 763
Chang, Y.-Y., van der Wel, A., Rix, H.-W., Wuyts, S., Zibetti, S., Ramkumar, B., & Holden, B. 2013, ApJ, 762, 83
Dekel, A., Sari, R., & Ceverino, D. 2009, ApJ, 703, 785
Emsellem, E., et al. 2011, MNRAS, 414, 888
Faber, S. M., et al. 2007, ApJ, 665, 265
Fall, S. M., & Frenk, C. S. 1983, AJ, 88, 1626
Franx, M., Illingworth, G., & de Zeeuw, T. 1991, ApJ, 383, 112
Galametz, A., et al. 2013, ApJS, 206, 10
Giavalisco, M., et al. 2004, ApJ, 600, L93
Guo, Y., Giavalisco, M., Ferguson, H. C., Cassata, P., & Koekemoer, A. M. 2012, ApJ, 757, 120
Guo, Yicheng, et al. 2013, ApJ, in press
Grogin, N. A., et al. 2011, ApJS, 197, 35
Holden, B. P., van der Wel, A., Rix, H.-W., & Franx, M. 2012, ApJ, 749, 96
Holden, B. P., et al. 2009, ApJ, 693, 617
Hopkins, P. F., Cox, T. J., Kereš, D., & Hernquist, L. 2008, ApJS, 175, 390
Hubble, E. P. 1926, ApJ, 64, 321
Khochfar, S., & Silk, J. 2006, ApJ, 648, L21
Kimm, T. & Yi, S. K. 2007, ApJ, 670, 1048
Koekemoer, A. M., et al. 2011, ApJS, 197, 36
Kormendy, J., & Bender, R. 1996, ApJ, 464, L119
Kriek, M., van Dokkum, P. G., Labbé, I., Franx, M., Illingworth, G. D., Marchesini, D., & Quadri, R. F. 2009, ApJ, 700, 221
Lambas, D. G., Maddox, S. J., & Loveday, J. 1992, MNRAS, 258, 404
Lawrence, A., et al. 2007, MNRAS, 379, 1599
Man, A. W. S., Toft, S., Zirm, A. W., Wuyts, S., & van der Wel, A. 2012, ApJ, 744, 85
Martig, M., Bournaud, F., Teyssier, R., & Dekel, A. 2009, ApJ, 707, 250
McGrath, E. J., Stockton, A., Canalizo, G., Iye, M., & Maihara, T. 2008, ApJ, 682, 303
Méndez-Abreu, J., Simonneau, E., Aguerri, J. A. L., & Corsini, E. M. 2010, A&A, 521, 71
Naab, T., Johansson, P. H., & Ostriker, J. P. 2009, ApJ, 699, L178
Newman, A. B., Ellis, R. S., Bundy, K., & Treu, T. 2012, ApJ, 746, 162
Oser, L., Naab, T., Ostriker, J. P., & Johansson, P. H. 2012, ApJ, 744, 63
Padilla, N. D., & Strauss, M. A. 2008, MNRAS, 388, 1321
Patel, S. G., Holden, B. P., Kelson, D. D., Franx, M., van der Wel, A., & Illingworth, G. D. 2012, ApJ, 748, L27
Peng, C. Y., Ho, L. C., Impey, C. D., & Rix, H.-W. 2010, AJ, 139, 2097
Rix, H.-W., & Zaritsky, D. 1995, ApJ, 447, 82
Robaina, A. R., Bell, E. F., van der Wel, A., Somerville, R. S., Skelton, R. E., McIntosh, D. H., Meisenheimer, K., & Wolf, C. 2010, ApJ, 719, 844
Ryden, B. 1992, ApJ, 396, 445
Ryden, B. S. 1996a, ApJ, 461, 146

—. 1996b, ApJ, 471, 822
Sandage, A., Freeman, K. C., & Stokes, N. R. 1970, ApJ, 160, 831
Stark, A. A. 1977, ApJ, 213, 368
Stockton, A., McGrath, E., & Canalizo, G. 2006, ApJ, 650, 706
Stockton, A., McGrath, E., Canalizo, G., Iye, M., & Maihara, T. 2008, ApJ, 672, 146
Toft, S., Franx, M., van Dokkum, P., Förster Schreiber, N. M., Labbe, I., Wuyts, S., & Marchesini, D. 2009, ApJ, 705, 255
Toft, S., et al. 2007, ApJ, 671, 285
Tremblay, B., & Merritt, D. 1995, AJ, 110, 1039
—. 1996, AJ, 111, 2243
van den Bosch, F. C., Aquino, D., Yang, X., Mo, H. J., Pasquali, A., McIntosh, D. H., Weinmann, S. M., & Kang, X. 2008, MNRAS, 387, 79
van der Wel, A., Bell, E. F., Holden, B. P., Skibba, R. A., & Rix, H.-W. 2010, ApJ, 714, 1779
van der Wel, A., Franx, M., Wuyts, S., van Dokkum, P. G., Huang, J., Rix, H.-W., & Illingworth, G. D. 2006, ApJ, 652, 97
van der Wel, A., Holden, B. P., Zirm, A. W., Franx, M., Rettura, A., Illingworth, G. D., & Ford, H. C. 2008, ApJ, 688, 48
van der Wel, A., Rix, H.-W., Holden, B. P., Bell, E. F., & Robaina, A. R. 2009, ApJ, 706, L120
van der Wel, A., & van der Marel, R. P. 2008, ApJ, 684, 260
van der Wel, A., et al. 2011, ApJ, 730, 38
—. 2012, ApJS, 203, 24
van Dokkum, P. G., et al. 2008, ApJ, 677, L5
Vincent, R. A., & Ryden, B. S. 2005, ApJ, 623, 137
Vulcani, B., et al. 2011, MNRAS, 413, 921
Whitaker, K. E., Kriek, M., van Dokkum, P. G., Bezanson, R., Brammer, G., Franx, M., & Labbé, I. 2012, ApJ, 745, 179
Williams, R. J., Quadri, R. F., Franx, M., van Dokkum, P., & Labbé, I. 2009, ApJ, 691, 1879
Wuyts, S., Labbé, I., Schreiber, N. M. F., Franx, M., Rudnick, G., Brammer, G. B., & van Dokkum, P. G. 2008, ApJ, 682, 985
Wuyts, S., et al. 2007, ApJ, 655, 51
—. 2011, ApJ, 742, 96
—. 2012, ApJ, 753, 114
Zirm, A. W., et al. 2007, ApJ, 656, 66